JCTC Journal of Chemical Theory and Computation

Article

Cite This: J. Chem. Theory Comput. 2020, 16, 302−313

pubs.acs.org/JCTC

Extending the Representation of Multistate Coupled Potential Energy Surfaces To Include Properties Operators Using Neural Networks: Application to the 1,2^{1}A States of Ammonia

Yafu Guan,*,† Hua Guo,*,‡ and David R. Yarkony*,†

†Department of Chemistry, Johns Hopkins University, Baltimore, Maryland 21218, United States

‡Department of Chemistry and Chemical Biology, University of New Mexico, Albuquerque, New Mexico 87131, United States

ABSTRACT: Fitting coupled adiabatic potential energy surfaces using coupled diabatic states enables, for accessible systems, nonadiabatic dynamics to be performed with unprecedented accuracy, when compared with on-the-fly dynamics. On-the-fly dynamics has advantages, not the least of which is the ability to compute molecular properties including electric dipole moments, transition dipole moments, and spin−orbit couplings. The availability of these terms extends the range of processes that can be treated with on-the-fly methods. In this work we use the example of fitting electric dipole and transition dipole moments of the 1,2^{1}A states of ammonia to show how to bring these advantages to the fit-coupled-surface method using a diabatic representation.

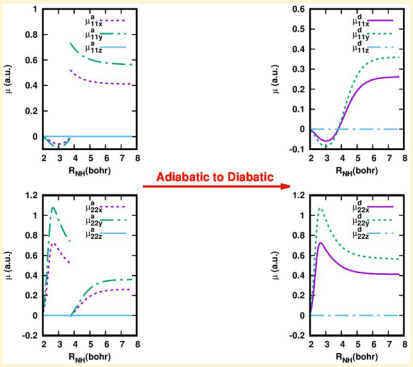

Downloaded via JOHNS HOPKINS UNIV on January 24, 2020 at 13:17:37 (UTC).
See https://pubs.acs.org/sharingguidelines for options on how to legitimately share published articles.

1. INTRODUCTION

The electronic structure data, energies, energy gradients, and derivative couplings needed for accurate quantum mechanical simulations of electronically nonadiabatic processes involving conical intersections[1,2] can be calculated "on the fly" as needed in direct dynamics or obtained from fit coupled surfaces that analytically represent these data. A major advantage of fit-coupled-surface methods is that more accurate electronic structure methods can be employed than are currently practical in direct dynamics. Once the surfaces are constructed, the computational cost of evaluating analytic electronic structure data is negligible compared to actual ab initio calculations, allowing long time dynamic simulations that are not practical in direct dynamics.

In electronic structure calculations, the auxiliary molecular properties including electric dipole moments and spin−orbit couplings are routinely obtained at limited cost from electronic wave functions once the eigenstates have been determined. They can be easily incorporated into on-the-fly methods,[3−5] which extends the range of processes that can be treated with these methods. By fitting auxiliary molecular properties, this advantage can also brought to fit-surface methods. There were previous attempts to fit auxiliary molecular properties in the adiabatic representation.[6−14] However, when it comes to nonadiabatic processes involving conical intersections, the adiabatic molecular properties cannot be fit due to the singularities attributable to the conical intersection seam, which renders them discontinuous in the space of nuclear coordinates. The easiest solution is to transform molecular properties to a diabatic representation, in which the discontinuities near conical intersections disappear. Diabatized molecular properties become smooth functions of nuclear coordinates and can thus be fit.[15] By fitting diabatized molecular properties, more chemical processes can be treated with the more accurate fit-surface methods.

Fitting diabatized molecular properties requires an accurate diabatic representation, in which the energies, energy gradients, derivative couplings, and local topography of the conical intersection seam should be well reproduced. For polyatomic molecules rigorous diabatic bases do not exist;[16−18] the more precise name for such a representation is quasi-diabatic representation.[19] The attribute *quasi* shall be omitted below except as needed for emphasis. Due to the fact that the quasi-diabatic representation is not uniquely defined, a variety of methods to construct diabatic representations have been reported in the literature. It remains a challenging task to construct the highly accurate diabatic representations needed to properly diabatize molecular properties. Currently available methods can be divided into four categories: property-based methods,[20,21] methods based on configuration uniformity,[22,23] diabatization by ansatz,[24,25] and derivative-coupling-based methods.[18] Among all these methods, the derivative-coupling-based methods are in principle the most accurate, as they use the derivative coupling information from electronic wave functions to diabatize the electronic states, so that the quality of diabatization can be quantifiably controlled through residual derivative couplings. The derivative coupling information is also important to the analysis of the geometric phase,[26−33] the local topology of conical intersections,[34,35] and

Received: September 10, 2019
Published: November 19, 2019

© 2019 American Chemical Society

DOI: 10.1021/acs.jctc.9b00898
J. Chem. Theory Comput. 2020, 16, 302−313

avoided-crossing regions.[36] Without using the derivative coupling information, the quality of diabatization depends to a large extent on the physical intuition for a specific system and is thus not strictly under control.[37] Previous derivative-coupling-based attempts reported in literature include solving the Poisson equation,[38−40] Shepard interpolation,[41−43] and line integral methods.[44,45] Recently, Zhu and Yarkony (ZY) introduced a diabatization procedure, in which the diabatic Hamiltonian is expressed in symmetry adapted polynomials and the ab initio electronic structure data including energies, energy gradients, and derivative couplings are simultaneously fit and diabatized (FaD) to generate a robust and accurate quasi-diabatic representation.[46−49] Since the ab initio determined derivative couplings are available, the residual derivative couplings can be determined and used to assess the quality of the diabatization so that the quality of diabatization is strictly under control. This approach ultimately provides an accurate, quantifiably quasi-diabatic representation in a least-squares sense. Its accuracy has been demonstrated by excellent agreement with experimentally measured dynamical attributes in photodissociation of ammonia.[50−53] More recently, a neural network extension of the ZY fitting method has been reported.[54,55]

Since an accurate quasi-diabatic representation for ammonia has been constructed with the ZY fitting method, ammonia is a good initial example of fitting auxiliary molecular properties in the diabatic representation to complement the fit-coupled potential energy surface methods. In this work, we are interested in fitting the electric dipole and transition dipole moment surfaces (DMSs) for the $1,2^1$A states of ammonia. The $1,2^1$A states are coupled by a conical intersection seam, which plays a central role in the nonadiabatic photodissociation of ammonia.

$$NH_3(\tilde{X}, \nu) \rightarrow NH_3(\tilde{A}, \nu') \rightarrow NH_2(\tilde{X}, \tilde{A}) + H \tag{1}$$

The electric dipole moments are important prerequisites for the theoretical prediction of molecular spectra. The diabatic dipole moment surfaces constructed in this work will provide a crucial ingredient for predicting the intensities of rotation−vibration transitions not only on a single adiabatic electronic state but also between different electronic states. Being a vector molecular property, dipole moments are more difficult to fit than energies.[77,78] Special treatment concerning the symmetry of translation, rotation, and permutation of identical nuclei and space fixed inversion is needed for the diabatization of electric dipole moments.

The rest of the paper is organized as follows: section 2 contains the details of the methods to fit diabatized electric dipole moments, in which a standard orientation for ammonia is introduced to simplify the treatment of symmetry, and a cluster growing algorithm with Gaussian process regression is employed to remove the arbitrariness in the sign of the transition dipole moments. In section 3, the fitting results are presented. Section 4 summarizes and suggests future directions to be pursued.

2. METHODS

2.1. Molecular Properties in Adiabatic and Diabatic Bases. At first, before fitting any diabatized properties, it is important to know how the molecular properties transform between the adiabatic and diabatic bases.

The adiabatic basis consists of N^{state} real-valued adiabatic electronic wave functions $\mathbf{\Psi}^{\text{a}}_k(\mathbf{r};\mathbf{R})$, $k = 1 - N^{\text{state}}$, which are eigenfunctions of the nonrelativistic Born−Oppenheimer Hamiltonian $\mathbf{H}^{\text{e}}(\mathbf{r};\mathbf{R})$:

$$\mathbf{H}^{\text{e}}(\mathbf{r};\ \mathbf{R})\ \mathbf{\Psi}^{\text{a}}_k(\mathbf{r};\ \mathbf{R}) = E_k(\mathbf{R})\ \mathbf{\Psi}^{\text{a}}_k(\mathbf{r};\ \mathbf{R}) \tag{2}$$

where $\mathbf{r}$ are electronic coordinates and $\mathbf{R}$ are nuclear coordinates; E_k is the adiabatic energy. The $\mathbf{\Psi}^{\text{a}}_k(\mathbf{r};\mathbf{R})$ are coupled via derivative couplings. The coupling between the kth and lth states $\mathbf{f}^{\text{a}}_{kl}(\mathbf{R})$ takes the following form:

$$\begin{aligned}\mathbf{f}^{\text{a}}_{kl}(\mathbf{R}) &\equiv \langle \mathbf{\Psi}^{\text{a}}_k(\mathbf{r};\ \mathbf{R})|\nabla_{\mathbf{R}}\mathbf{\Psi}^{\text{a}}_l(\mathbf{r};\ \mathbf{R})\rangle_{\mathbf{r}} \\ &= \frac{\langle \mathbf{\Psi}^{\text{a}}_k(\mathbf{r};\ \mathbf{R})|\nabla_{\mathbf{R}}\mathbf{H}^{\text{e}}|\mathbf{\Psi}^{\text{a}}_l(\mathbf{r};\ \mathbf{R})\rangle_{\mathbf{r}}}{E_l(\mathbf{R}) - E_k(\mathbf{R})}\end{aligned} \tag{3}$$

$\mathbf{f}^{\text{a}}_{kl}(\mathbf{R})$ is singular when the kth and lth states are degenerate, making adiabatic basis very difficult to use when degeneracy occurs. The degeneracy also leads to discontinuity in adiabatic energies and molecular properties. The traditional way of resolving this problem is to replace adiabatic basis with diabatic basis in which the derivative couplings are negligible, and the discontinuity in energies and molecular properties will also disappear in general.[15]

Adiabatic and diabatic bases are linked to each other via an orthogonal transformation:

$$\mathbf{\Psi}^{\text{a}}_k(\mathbf{r};\ \mathbf{R}) = \sum_{j=1}^{N^{\text{state}}} D_{jk}(\mathbf{R})\ \mathbf{\Psi}^{\text{d}}_j(\mathbf{r};\ \mathbf{R}) \tag{4}$$

where D_{jk} is the element of the orthogonal matrix $\mathbf{D}$, which is called the adiabatic-to-diabatic (AtD) transformation. The derivative couplings of adiabatic and diabatic states are linked by the relation

$$\mathbf{f}^{\text{a}} = \mathbf{D}^{\text{T}}\mathbf{f}^{\text{d}}\mathbf{D} + \mathbf{D}^{\text{T}}\nabla_{\mathbf{R}}\mathbf{D} \equiv \mathbf{D}^{\text{T}}\mathbf{f}^{\text{d}}\mathbf{D} + \mathbf{f}(\mathbf{D}) \tag{5}$$

In eq 5 and below we will suppress the $\mathbf{R}$ dependence of a quantity when no confusion will result. For $N^{\text{state}} = 2$, $\mathbf{D}$ has the form

$$\mathbf{D} = \begin{pmatrix} \cos\theta(\mathbf{R}) & -\sin\theta(\mathbf{R}) \\ \sin\theta(\mathbf{R}) & \cos\theta(\mathbf{R}) \end{pmatrix} \tag{6}$$

where $\theta(\mathbf{R})$ is called the rotation angle. Equation 5 then becomes

$$\mathbf{f}^{\text{a}}_{ij} = \mathbf{f}^{\text{d}}_{ij} - \nabla_{\mathbf{R}}\theta \tag{7}$$

The goal of AtD transformation is to have $\mathbf{f}^{\text{d}}_{ij} = \mathbf{0}$; then eq 7 becomes

$$\nabla_{\mathbf{R}}\theta = -\mathbf{f}^{\text{a}}_{ij} \tag{8}$$

Consider a Hermitian molecular property operator A; its matrix form in adiabatic and diabatic bases would be

$$A^{\text{a}}_{ij}(\mathbf{R}) = \langle \mathbf{\Psi}^{\text{a}}_i(\mathbf{r};\ \mathbf{R})|A|\mathbf{\Psi}^{\text{a}}_j(\mathbf{r};\ \mathbf{R})\rangle_{\mathbf{r}} \tag{9}$$

$$A^{\text{d}}_{ij}(\mathbf{R}) = \langle \mathbf{\Psi}^{\text{d}}_i(\mathbf{r};\ \mathbf{R})|A|\mathbf{\Psi}^{\text{d}}_j(\mathbf{r};\ \mathbf{R})\rangle_{\mathbf{r}} \tag{10}$$

$\mathbf{A}^{\text{a}}$ and $\mathbf{A}^{\text{d}}$ are linked by the same orthogonal matrix:

$$\mathbf{A}^{\text{a}} = \mathbf{D}^{\text{T}}\mathbf{A}^{\text{d}}\mathbf{D} \tag{11}$$

If A is replaced with $\mathbf{H}^{\text{e}}$, then we have

$$[\mathbf{H}^{\text{d}}(\mathbf{R}) - \mathbf{I}E^{\text{a},j,(\text{m})}(\mathbf{R})]\mathbf{d}^{j}(\mathbf{R}) = \mathbf{0} \tag{12}$$

DOI: 10.1021/acs.jctc.9b00898
J. Chem. Theory Comput. 2020, 16, 302−313

Table 1. Character Table of $D_{3h}(M)$[a]

	E	(123), (132)	(12), (23), (13)	E^*	(123)*, (132)*	(12)*, (23)*, (13)*
A_1'	1	1	1	1	1	1
A_1''	1	1	1	−1	−1	−1
A_2'	1	1	−1	1	1	−1
A_2''	1	1	−1	−1	−1	1
E'	2	−1	0	2	−1	0
E''	2	−1	0	−2	1	0

[a]The star symbol (∗) denotes inversion of all nuclei and electrons.

$\mathbf{H}^d$ is the diabatic Hamiltonian, also known as the diabatic potential energy matrix (PEM), $\mathbf{H}^a$ is diagonal in the adiabatic basis, $E^{a,j,(m)}$ is the adiabatic energy of the jth electronic state, and $\mathbf{d}^j$ is the jth column of $\mathbf{D}$. Therefore, the orthogonal matrix $\mathbf{D}$ can be obtained by diagonalizing $\mathbf{H}^d$ with only the sign of each column of $\mathbf{D}$ undetermined. Before fitting any diabatized molecular properties, we assume that the diabatic Hamiltonian is already constructed. In the work, we will fit the diabatized electric dipole moment $\boldsymbol{\mu}^d$, where

$$\boldsymbol{\mu}^d = \mathbf{D}\boldsymbol{\mu}^a\mathbf{D}^T \quad \text{or} \quad \boldsymbol{\mu}^a = \mathbf{D}^T\boldsymbol{\mu}^d\mathbf{D} \tag{13}$$

It is important to note that the electric dipole moment operator depends on both the locations and charges of the electrons ($\mathbf{r}_i$, $-e$) and the locations and charges of the nuclei ($\mathbf{R}_I$, $Z_I e$):

$$\boldsymbol{\mu} = -e\sum_i \mathbf{r}_i + e\sum_I Z_I\mathbf{R}_I = \boldsymbol{\mu}_e + \boldsymbol{\mu}_N \tag{14}$$

where $\boldsymbol{\mu}_e$ and $\boldsymbol{\mu}_N$ denote the electronic and nuclear parts of electric dipole moment operator, respectively.

2.2. Complete Nuclear Permutation Inversion (CNPI) Symmetry of Diabatized Dipole Moments. The DMSs will cover all the energy-accessible regions of the photodissociation of ammonia; thus the CNPI group will be used. Assuming the electronic character of a diabatic state does not change, the CNPI symmetry of diabatized dipole moment can be analyzed through the following equation:

$$\boldsymbol{\mu}_{ij}^d = \langle\boldsymbol{\Psi}_i^d|\boldsymbol{\mu}|\boldsymbol{\Psi}_j^d\rangle_{\mathbf{r}} \tag{15}$$

It is clear from above that the dipole has a matrix form, and each individual block (dipole matrix element) $\boldsymbol{\mu}_{ij}^d$ carries the irreducible representation corresponding to irred($\boldsymbol{\Psi}_i^d$) × irred($\boldsymbol{\mu}$) × irred($\boldsymbol{\Psi}_j^d$), where "irred" denotes "the irreducible representation carried by". The CNPI group pertaining to ammonia is $\mathbf{G}_{12}$, also denoted as $\mathbf{D}_{3h}(M)$.[56] Table 1 provides the character table of $\mathbf{D}_{3h}(M)$. The two diabatic states carry A_1' and A_2'' irreducible representations, respectively.[46] In the space-fixed Cartesian frame, the electric dipole moment operator $\boldsymbol{\mu}$ will carry the A_1'' irreducible representation. Then correspondingly, the three blocks of diabatized dipole moment matrix $\boldsymbol{\mu}_{11}^d$, $\boldsymbol{\mu}_{22}^d$, and $\boldsymbol{\mu}_{12}^d$ will carry A_1'', A_1'', and A_2' irreducible representations, respectively.

Since ammonia is a neutral molecule, the total electric dipole moment will be invariant with respect to translation. Still, one needs to design a special functional form to account for the rotation and CNPI symmetry. However, by placing geometries at a standard orientation, we will restrict the fitting to a certain arrangement of geometries and the functional form for fitting will also be significantly simplified.

2.3. Standard Orientation. For ammonia, the following standard orientation will be used, which also defines a body-fixed Cartesian frame.[7] The unit vectors for the body-fixed frame are denoted as $\mathbf{e}_x$, $\mathbf{e}_y$, and $\mathbf{e}_z$. First, the three hydrogen atoms are permuted to have $R_{NH_1} \le R_{NH_2} \le R_{NH_3}$. Then, with N set as the origin, H_1 is placed on the positive x-axis; i.e., the shortest NH bond is along the x-axis. The positive z-axis is set to be along the direction of $\mathbf{R}_{NH_1} \times \mathbf{R}_{NH_2}$, and $\mathbf{e}_y$ is the cross product of $\mathbf{e}_z$ and $\mathbf{e}_x$. Figure 1 presents the definition of this

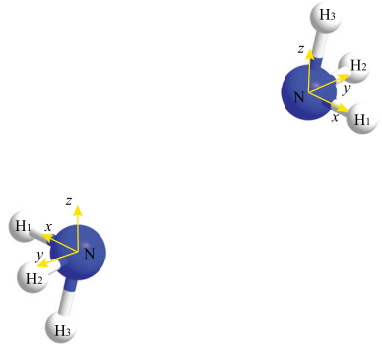

Figure 1. Body-fixed Cartesian frame for NH_3. Two ammonia geometries are shown, and they are related by inversion operation.

body-fixed Cartesian frame and how the coordinates transform when the geometry is inverted. It is easy to see that the x and y coordinates of H nuclei in the body-fixed frame remain the same in the inverted geometry of NH_3; however, the z coordinates will have a sign change. Therefore, we can conclude that the x and y coordinates in the body-fixed frame are symmetric with respect to inversion of the whole molecule, whereas the z coordinate is antisymmetric. According to eq 15, the symmetry of each component of diabatized dipole moments in this body-fixed frame with respect to inversion can be obtained, and symmetries are listed in Table 2. The body-fixed frame defined above is problematic

Table 2. Symmetries of x, y, and z Components of Diabatized Dipole Moments in the Body-Fixed Frame with Respect to Inversion of NH_3

	x component	y component	z component
$\boldsymbol{\mu}_{11}^d$	symmetric	symmetric	antisymmetric
$\boldsymbol{\mu}_{22}^d$	symmetric	symmetric	antisymmetric
$\boldsymbol{\mu}_{12}^d$	antisymmetric	antisymmetric	symmetric

when N, H_1, and H_2 are collinear or nearly collinear. At such geometries, $\mathbf{e}_z$ is not well-defined. Fortunately, these geometries are rare and can be excluded from fitting. The body-fixed Cartesian frame and the original Cartesian frame are linked by the three-dimensional (3D) rotation matrix ($\mathbf{e}_x$, $\mathbf{e}_y$, $\mathbf{e}_z$).

DOI: 10.1021/acs.jctc.9b00898
J. Chem. Theory Comput. 2020, 16, 302−313

Placing geometries to the standard orientation restricts the fitting of dipole moments to only a specific portion of configuration space. First, the ascending bong length condition restricts the fitting to only one ordering of hydrogen atoms. The dipole moments of the other orderings can be easily obtained through permutation symmetry, which is given in section 2.2. Second, the body-fixed frame helps to get rid of translational and rotational degrees of freedom. Dipole moments in the body-fixed frame are functions of internal coordinates alone. Therefore, in this specific portion of configuration space, the diabatized dipole moments are smooth functions of internal coordinates. The functional form used to fit the diabatized dipole moments will thus be greatly simplified.

2.4. A Cluster Growing Algorithm Removes the Arbitrariness in the Sign of the Transition Dipole Moment. The sign of the adiabatic transition dipole moment from ab initio calculations is arbitrary. This arbitrariness could make the resulting diabatized dipole moments discontinuous. In this work, a cluster growing algorithm is used to achieve sign consistency.[57] First, an initial cluster of points with correct sign assignments made by hand is assembled. Then the diabatized dipole moments of the current cluster are fit by Gaussian process regression (GPR).[58] The GPR model is then used to determine the signs of nearby points. The newly determined points are added into the cluster, and a new iteration is performed. After each iteration, the cluster grows, hence the name "cluster growing algorithm".

The success of the cluster growing algorithm hinges on the smoothness of the diabatized properties that are being fit and the capability of the GPR model to extrapolate. The smoothness of the diabatized properties, a premise of this work, can be assumed provided that the diabatic representation in use is smooth and there are very few bad points in the ab initio calculations. Using a physically motivated functional form to fit diabatic properties would help the model to extrapolate better. However, for complex systems, coming up with a suitable and accurate functional form is tedious and is not an easy task. Furthermore, it is not a universal solution and varies from system to system. In this work, GPR is used, which provides a flexible framework for probabilistic regression and is widely used to solve high-dimensional, nonlinear regression problems. Most importantly, it also shows the capability to extrapolate.[59] The details of the cluster growing algorithm with GPR can be seen in Appendix A.

2.5. Diabatized Dipole Moment Fit Surfaces with Neural Networks. Along with the sign consistency obtained by the cluster growing algorithm, the diabatized DMSs with GPR are simultaneously obtained. However, in ab initio calculations, bad points with abrupt changes may occur even in the absence of conical intersections, which would result in discontinuities in diabatized properties. Due to the high dimensionality of nuclear coordinate space, such discontinuities are difficult to detect, which may cause wrong sign assignments in the cluster growing algorithm. A wrong sign determination will lead to a cascade of more wrong signs. Therefore, the diabatized DMSs with GPR could be problematic. Moreover, GPR cannot deal with symmetry properly. For example, some components of diabatized dipole moments at the standard orientation are antisymmetric with respect to inversion, which means that they are zero at geometries that are invariant with respect to inversion. GPR cannot exactly reproduce zero values at these geometries due to the existence of fitting errors, which can also result in discontinuities near such geometries.

However, if the diabatized dipole moments with proper sign assignment can be accurately fit with smooth symmetric functional forms, the resulting DMSs should be reliable. Therefore, we refit the diabatized dipole moments with smooth artificial neural network (NN) functions. NNs have been used as a robust and powerful fitting tool. They provide flexible functional forms to represent scattered data as accurately as possible.[60,61] Special NN functional forms to account for symmetry can also be designed, which is not allowed in GPR. In this work, the simple feed-forward NN is employed, the definition and structure of which were reported previously.[54] The diabatized dipole moments at standard orientation are smooth functions of internal coordinates. In this work, the six inverse internuclear distances (denoted $1/\mathbf{R}$), which are symmetric with respect to inversion, are used to describe the symmetric components and thus are the input to the NN. As for antisymmetric components, the following functional form is used:

$$Q^{(3)}_{\mathrm{NHHH}} \cdot \mathrm{NN}(1/\mathbf{R}) \tag{16}$$

where

$$Q^{(3)}_{\mathrm{NHHH}} = \frac{(\mathbf{R}_{\mathrm{N}} - \mathbf{R}_{\mathrm{H}_1}) \cdot (\mathbf{R}_{\mathrm{N}} - \mathbf{R}_{\mathrm{H}_2}) \times (\mathbf{R}_{\mathrm{N}} - \mathbf{R}_{\mathrm{H}_3})}{r_{\mathrm{NH}_1} r_{\mathrm{NH}_2} r_{\mathrm{NH}_3}}$$

is an internal coordinate that is antisymmetric with respect to inversion.[46,62] The functional forms for all components of diabatized dipole moments (see Table 2) are

$$\begin{aligned}
\mu^{\mathrm{d}}_{11x} &= \mathrm{NN}_1(1/\mathbf{R}) \\
\mu^{\mathrm{d}}_{11y} &= \mathrm{NN}_2(1/\mathbf{R}) \\
\mu^{\mathrm{d}}_{11z} &= Q^{(3)}_{\mathrm{NHHH}} \mathrm{NN}_3(1/\mathbf{R}) \\
\mu^{\mathrm{d}}_{12x} &= Q^{(3)}_{\mathrm{NHHH}} \mathrm{NN}_4(1/\mathbf{R}) \\
\mu^{\mathrm{d}}_{12y} &= Q^{(3)}_{\mathrm{NHHH}} \mathrm{NN}_5(1/\mathbf{R}) \\
\mu^{\mathrm{d}}_{12z} &= \mathrm{NN}_6(1/\mathbf{R}) \\
\mu^{\mathrm{d}}_{22x} &= \mathrm{NN}_7(1/\mathbf{R}) \\
\mu^{\mathrm{d}}_{22y} &= \mathrm{NN}_8(1/\mathbf{R}) \\
\mu^{\mathrm{d}}_{22z} &= Q^{(3)}_{\mathrm{NHHH}} \mathrm{NN}_9(1/\mathbf{R})
\end{aligned} \tag{17}$$

The functional forms defined in eq 17 are very simple in the sense that no complicated symmetrized internal coordinates such as permutation invariant polynomials[63,64] are used. For a given geometry, its diabatized dipole and transition dipole moments at standard orientation can be readily obtained from these functions. By using the inverse of the relations to the standard orientation, the (adiabatic or diabatized) dipole and transition dipole moments at the original geometry can also be easily obtained.

The NN training optimizes the NN parameters to minimize the following performance index:

DOI: 10.1021/acs.jctc.9b00898
J. Chem. Theory Comput. 2020, 16, 302−313

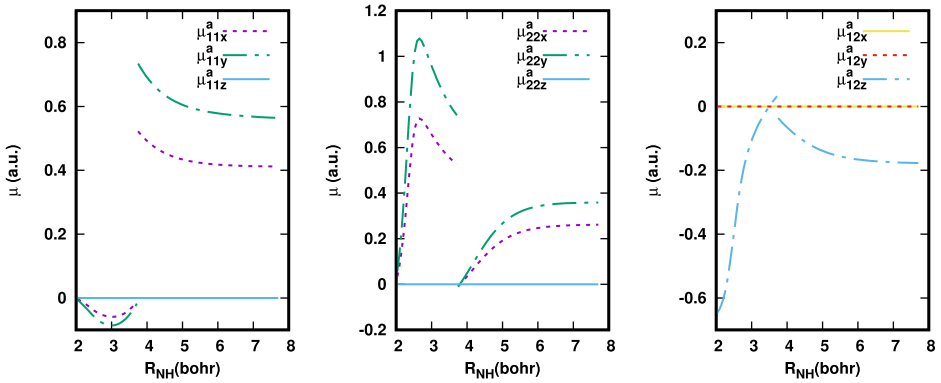

Figure 2. Adiabatic dipole moments $\boldsymbol{\mu}^{a}_{11}$, $\boldsymbol{\mu}^{a}_{22}$, and $\boldsymbol{\mu}^{a}_{12}$ along the planar dissociation path. The arbitrary signs of $\boldsymbol{\mu}^{a}_{12}$ have been manually adjusted.

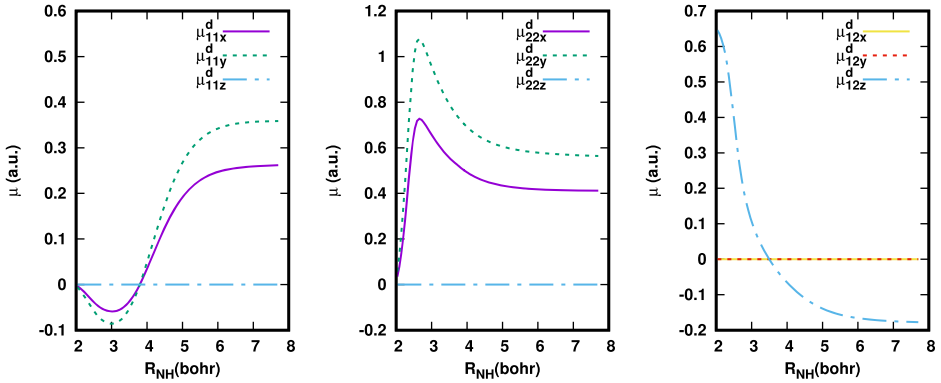

Figure 3. Diabatized dipole moments $\boldsymbol{\mu}^{d}_{11}$, $\boldsymbol{\mu}^{d}_{22}$, and $\boldsymbol{\mu}^{d}_{12}$ along the dissociation path.

$$P(\boldsymbol{\theta}) = \frac{1}{2}\sum_{q=1}^{Q}\sum_{i=1}^{N^{state}}\sum_{j=i}^{N^{state}}\sum_{k=x,y,z}\{(\mu^{d,(m)}_{ijkq} - \mu^{d}_{ijkq})^2 + [w(\mu^{a,(m)}_{ijkq} - \mu^{a,(ab)}_{ijkq})]^2\} + \frac{1}{2}t\boldsymbol{\theta}^{\dagger}\boldsymbol{\theta} \quad (18)$$

where w is a connecting weight, Q is the number of geometries, $\mu^{d,(m)}_{ijkq}$ represents the NN model diabatized dipole moments, μ^{d}_{ijkq} represents the diabatized dipole matrix elements with proper sign assignments, $\mu^{a,(m)}_{ijkq}$ represents the adiabatic dipole moments obtained from the NN model, and $\mu^{a,(ab)}_{ijkq}$ represents ab initio dipole moments. Also, $\frac{1}{2}t\boldsymbol{\theta}^{\dagger}\boldsymbol{\theta}$ is the regularization term that prevents overfitting, where t is a small positive factor. The regularization term reduces the complexity of the NN model and can help generate smooth NN functions. The Levenberg–Marquardt algorithm which is used to minimize the performance index is very numerically robust and can achieve convergence very quickly.[65]

3. RESULTS

3.1. Adiabatic and Diabatized Dipole Moments. The ab initio data including energies, energy gradients, and derivative couplings for ammonia were those used in the previous ZY fitting of a diabatic Hamiltonian,[66] and the corresponding diabatic PEM will be denoted as NH3ZY. The electric dipole and transition dipole moments are obtained from the same multireference single and double excitation configuration (MRCISD) wave functions. The details of the MRCISD expansion have been reported previously.[46] All electronic structure calculations reported in this work were performed using the COLUMBUS suite of electronic structure codes.[67,68] The AtD transformation for each geometry is obtained by diagonalizing the corresponding NH3ZY PEM. In this subsection, all the dipole moments are shown in the body-fixed frame defined in section 2.

Figures 2 and 3 present the adiabatic and diabatized dipole moments along the planar dissociation path connecting the minimum energy point on the 2^1A potential energy surface to the saddle point on that surface, the saddle point to the minimum energy crossing point (MEX) on the $1,2^1$A states conical intersection seam, and the seam point to the product channel. This path is essential for the description of the nonadiabatic photodissociation of ammonia, the potential energy curves for which are shown in Figure 4. All the geometries on the path are coplanar, which are inversion invariant. Thus, in Figure 2, μ^{a}_{11z}, μ^{a}_{22z}, μ^{a}_{12x}, and μ^{a}_{12y} are zero. The other components, however, exhibit a discontinuity at the conical intersection. On the other hand, after AtD transformation with eq 13, the discontinuities disappear in Figure 3, rendering all the diabatized dipole moments smooth.

Figure 5 provides an alternative picture of the diabatized dipole moments, plotting each component of the diabatized dipole moments as a function of R_{NH} and out-of-plane angle on a two-dimensional (2D) grid, where the reference geometry is the minimum of the 1^1A state (C_{3v}) and θ is the angle between the dissociative N–H bond and the C_3-axis. The corresponding 2D cut of adiabatic potential energy surface is shown in Figure 6, in which a conical intersection can be observed. Despite the presence of the conical intersection, the smoothness of the diabatized dipole moments is evident.

It is important to note that the signs of adiabatic transition dipole moments have been manually adjusted to make diabatized dipole moments smooth with eq 13 as seen in

DOI: 10.1021/acs.jctc.9b00898
J. Chem. Theory Comput. 2020, 16, 302–313

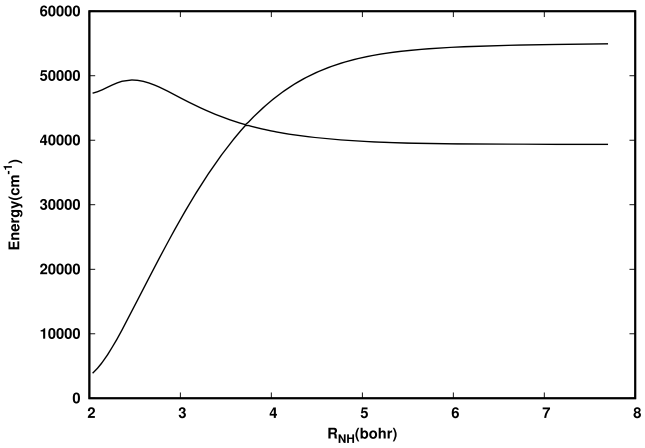

Figure 4. Potential energies of the 1,2^{1}A states as a function of R_{NH} along the dissociation path. A conical intersection (MEX) can be observed.

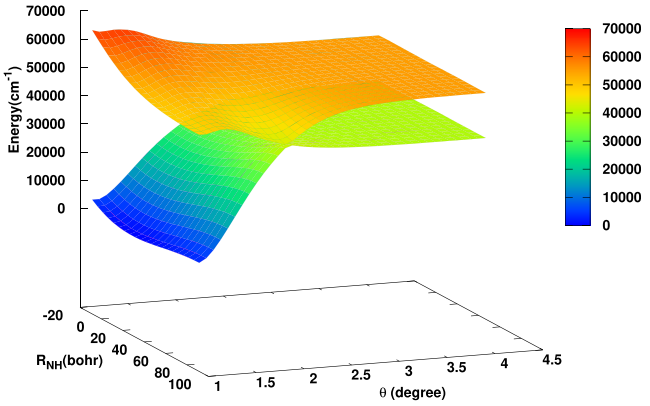

Figure 6. Potential energies of the 1,2^{1}A states as a function of R_{NH} and out-of-plane angle θ on a 2D grid. A conical intersection can be observed.

Figures 3 and 5. Sign consistency in the diabatic representation was already obtained on the 2D grid and along the dissociation path, which form the initial cluster for the cluster growing process.

3.2. Exclusion of Quasi-Degenerate Points in Cluster Growing Algorithm. The initial cluster consists of 347 points, which provides a basic description of the photodissociation of ammonia. The extension of the domain of the DMSs is then achieved by the cluster growing process with GPR. The Matérn kernel function of automatic relevance determination with $\nu = 5/2$ is used.[58] To obtain optimal kernel parameters, a limited memory quasi-Newton algorithm[69] is employed to maximize the log marginal likelihood (see Appendix A for details).

The NH3ZY PEM was obtained by a least-squares fitting, which is very accurate in terms of reproducing the ab initio data. However, differences are inevitable between ab initio results and corresponding predictions of the NH3ZY PEM. Most importantly, the location of the ab initio conical intersection seam was not exactly reproduced by the NH3ZY PEM. For example, the NH3ZY PEM predicts an energy difference of 48.3 cm^{-1} at MEX, which is supposed to be exactly zero. According to eq 8, the AtD transformation changes very rapidly near a conical intersection; this mismatch between ab initio dipole moment and AtD transformation will result in discontinuities of the diabatized dipole moment. The cluster growing algorithm may fail when it explores the vicinity of the conical intersection seam. Therefore, the quasi-degenerate points with energy differences less than a predefined threshold were excluded from the cluster growing process. In this work, the threshold is set to 300 cm^{-1}, which is about the largest mean unsigned error of the NH3ZY PEM.[55]

The signs of 2652 points were determined by the cluster growing algorithm. A total of 3003 points were ensembled to fit the diabatized DMSs.

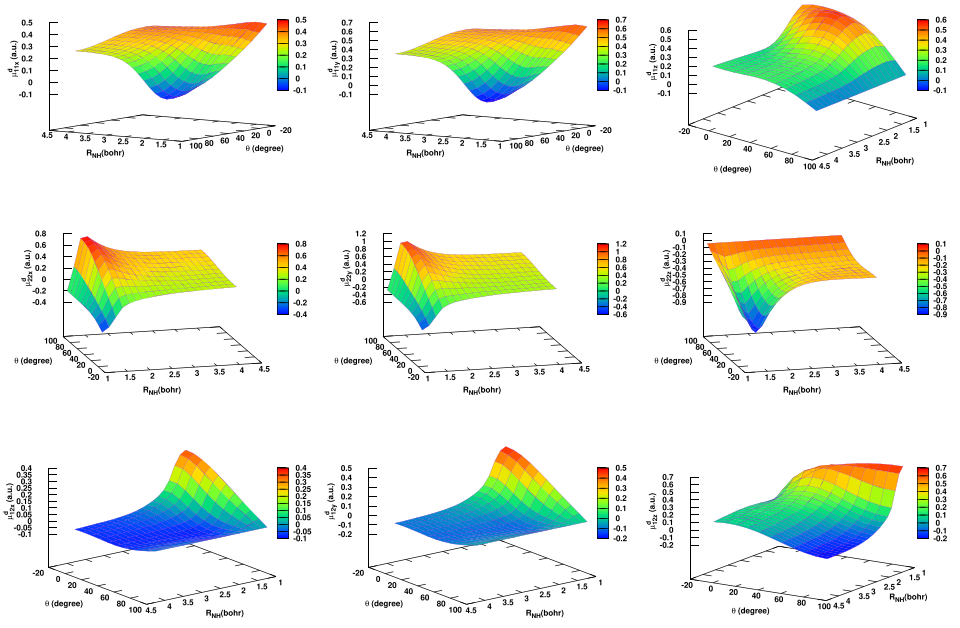

Figure 5. Nine components of diabatized dipole moments as functions of R_{NH} and out-of-plane angle θ on a 2D grid.

DOI: 10.1021/acs.jctc.9b00898
J. Chem. Theory Comput. 2020, 16, 302−313

3.3. Neural Network Dipole Moment Surfaces. The structure of the feed-forward NN used to refit diabatized dipole moments is 6−60−60−9, which means that this NN takes 6 inverse internuclear distances as input, has two hidden layers, both of which have 60 neurons, and gives an output with 9 components corresponding to NN_i (i = 1−9) in eq 17. The transfer function in the first and second layers is a hyperbolic tangent function $f(x) = \tanh(x)$; in the third layer, it is a linear function $f(x) = x$. w is set to 1×10^{-6}, and $t = 1 \times 10^{-6}$. Fifty trainings with different initial parameters were performed.

Table 3. Ten NN Fitting Results with Smallest RMSE[a]

no.	RMSE[d] (%)	RMSE[a] (%)
1	7.15	5.59
2	7.14	5.67
3	7.25	5.86
4	7.23	5.94
5	6.94	5.96
6	7.16	5.98
7	7.33	5.99
8	8.02	6.02
9	7.12	6.06
10	7.64	6.10

Table 3 lists 10 fitting results with the smallest root-mean-square error of adiabatic dipole moments (RMSE[a]). RMSE[a] is defined as

$$\mathrm{RMSE}^{\mathrm{a}} = \sqrt{\frac{\sum_{q=1}^{Q}\sum_{i=1}^{N^{\mathrm{state}}}\sum_{j=i}^{N^{\mathrm{state}}}\sum_{|\boldsymbol{\mu}_{ijq}^{\mathrm{a,(ab)}}|\geq 0.01\,\mathrm{au}}[|\boldsymbol{\mu}_{ijq}^{\mathrm{a,(m)}} - \boldsymbol{\mu}_{ijq}^{\mathrm{a,(ab)}}|/|\boldsymbol{\mu}_{ijq}^{\mathrm{a,(ab)}}|]^2}{N^{\mathrm{a}}}} \quad (19)$$

Only dipole or transition dipole moments with norms no less than 0.01 au will enter the error analysis, and N^{a} is the number of such dipole or transition dipole moments. Similarly, we have the definition of root-mean-square error of diabatized dipole moments (RMSE[d])

$$\mathrm{RMSE}^{\mathrm{d}} = \sqrt{\frac{\sum_{q=1}^{Q}\sum_{i=1}^{N^{\mathrm{state}}}\sum_{j=i}^{N^{\mathrm{state}}}\sum_{|\boldsymbol{\mu}_{ijq}^{\mathrm{d}}|\geq 0.01\,\mathrm{au}}[|\boldsymbol{\mu}_{ijq}^{\mathrm{d,(m)}} - \boldsymbol{\mu}_{ijq}^{\mathrm{d}}|/|\boldsymbol{\mu}_{ijq}^{\mathrm{d}}|]^2}{N^{\mathrm{d}}}} \quad (20)$$

RMSE[a] converged around 6% and RMSE[d] converged around 7%. The reasonably small fitting errors indicate that the diabatized dipole moments are smooth enough to be fit by smooth NN functions. The final diabatized DMSs are chosen as the average of these 10 fits. By averaging multiple results, more accurate DMSs can be obtained.[70−73] The RMSE[a] and RMSE[d] for final DMSs are 3.85 and 4.82%.

Even though we have fitted the diabatized DMSs, the adiabatic dipole moments may also be needed in practical calculations. For an arbitrary geometry, the diabatized dipole moments at a standard orientation can be readily obtained through diabatized DMSs. By using eq 13, the adiabatic dipole moments at the standard orientation can be obtained. Through a simple 3D rotation (i.e., multiplied by the matrix $(\mathbf{e}_x, \mathbf{e}_y, \mathbf{e}_z)$), the adiabatic dipole moments at the original orientation are obtained. One still needs to permute the H nuclei and translate the whole molecule to get back to the original geometry. However, considering that the electric dipole moment operator is invariant with respect to permutation of H nuclei and that ammonia is a neutral molecule, the adiabatic dipole moments of ammonia are thus invariant with respect to translation and permutations of H nuclei. Therefore, adiabatic dipole moments at the original geometry are already obtained after the 3D rotation.

In eq 12, the sign of eigenvector $\mathbf{d}^j$ is arbitrary, which makes the sign of the transition dipole obtained through eq 13 undetermined. The signs of the NN model determined transition dipoles have to be adjusted so that they can be compared to ab initio counterparts. Figure 7 shows the global accuracy of the NN model, comparing the NN model determined dipole moments and the ab initio dipole moments for $\boldsymbol{\mu}_{11}$, $\boldsymbol{\mu}_{22}$, and $\boldsymbol{\mu}_{12}$, respectively. In all three panels, the x-axis is the ab initio value and the y-axis is the NN model determined value. All the points lie near the lines $y = \pm x$, which indicates the NN model that can reproduce ab initio dipole moments very well. The signs of transition dipole moments are arbitrary; therefore, there are points that lie near the line $y = -x$ in the right panel for $\boldsymbol{\mu}_{12}$. Figure 8 shows the direct comparison between ab initio and NN model determined adiabatic dipole moments at the standard orientation along the same planar dissociation path as in Figures 2 and 3. As can be seen, the agreement is quite satisfactory, and the discontinuity at MEX is also reproduced.

In the cluster growing process, the quasi-degenerate points were excluded. One may raise concerns about the reliability of the diabatized dipole moment surface in the quasi-degenerate region due to the lack of these data points. Considering the fact that the seam space is $N^{\mathrm{int}} - 2$-dimensional, the smoothness of the diabatized dipole moments facilitates the

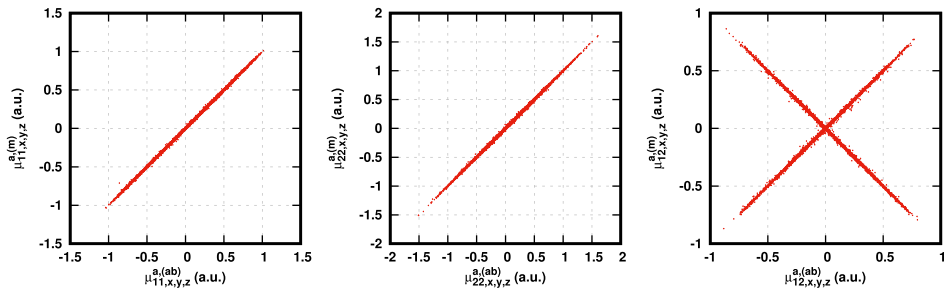

Figure 7. Comparison of ab initio and NN model determined adiabatic dipole moments. x-axis is the ab initio value; y-axis is the NN model determined value. The left, middle, and right panels show the results for $\boldsymbol{\mu}_{11}$, $\boldsymbol{\mu}_{22}$, and $\boldsymbol{\mu}_{12}$, respectively.

DOI: 10.1021/acs.jctc.9b00898
J. Chem. Theory Comput. 2020, 16, 302−313

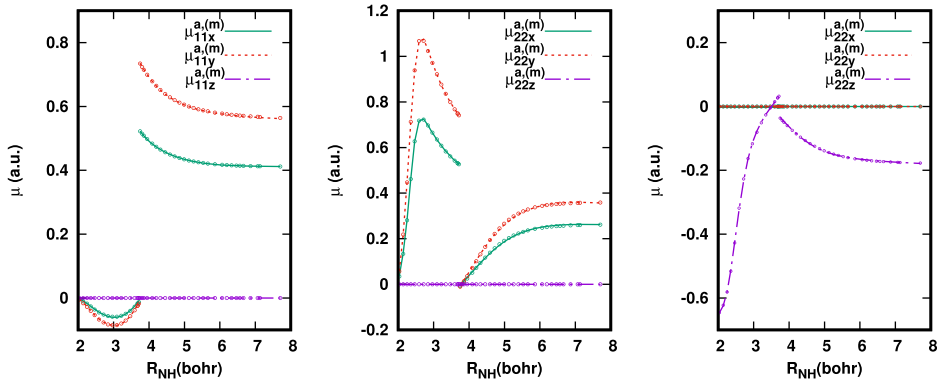

Figure 8. Direct comparison of ab initio (symbols) and NN model determined adiabatic dipole moments (lines) on the dissociation path. The left, middle, and right panels show the results for $\boldsymbol{\mu}_{11}$, $\boldsymbol{\mu}_{22}$, and $\boldsymbol{\mu}_{12}$, respectively. The arbitrary signs of transition dipole moments are manually adjusted.

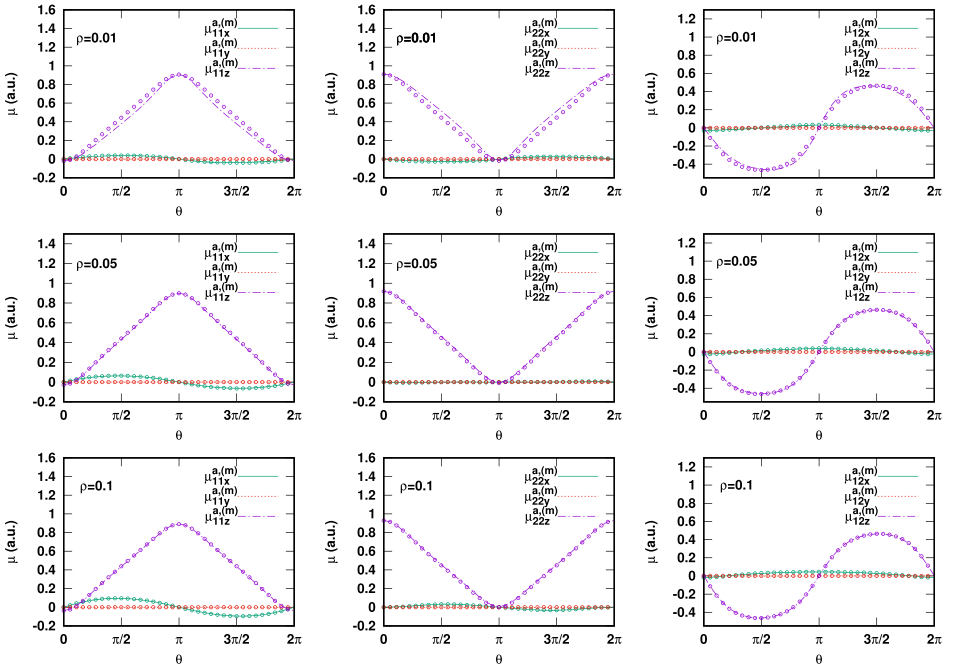

Figure 9. Comparison of ab initio (symbols) and NN model determined adiabatic dipole moments (lines) on the $g-h$ plane of MEX. The arbitrary signs of adiabatic transition dipole moments have been manually adjusted to achieve smoothness. Adiabatic dipole moment curves in the range $\theta \in [0, 2\pi]$ with three different ρ values (0.01 in upper row, 0.05 in middle row, and 0.1 in bottom row) are shown.

interpolation of N^{int}-dimensional NN model in a finite volume surrounding the seam. Therefore, the effect of exclusion of quasi-degenerate points should not be too serious. Figure 9 demonstrates how the NN adiabatic dipole moments behave near the MEX. The orthogonal intersection adapted coordinates based on $\mathbf{g}^{1,2}$ and $\mathbf{h}^{1,2}$ are used to describe the vicinity of the MEX,[35,74] where $\mathbf{g}^{1,2}$ is the energy difference gradient vector and $\mathbf{h}^{1,2}$ is the interstate coupling vector between the 1,2 ^{1}A states. In these coordinates, the x-axis is set to be parallel to $\mathbf{g}^{1,2}$ and the y-axis is parallel to $\mathbf{h}^{1,2}$. On the (x, y) plane, i.e., the $g-h$ plane, the degeneracy is lifted linearly. The polar coordinates (ρ, θ) with $(x, y) = (\rho \cos\theta, \rho \sin\theta)$ on the $g-h$ plane are used to plot the adiabatic dipole moments, where the unit vectors on the plane $\mathbf{e}_x$ and $\mathbf{e}_y$ are $\mathbf{g}^{1,2}/\|\mathbf{g}^{1,2}\|$ and $\mathbf{h}^{1,2}/\|\mathbf{h}^{1,2}\|$, respectively. In Figure 9, the adiabatic dipole moment curves in the range $\theta \in [0, 2\pi]$ with three different ρ values (0.01, 0.05, and 0.1) are shown. In general, the smoothness of the NN adiabatic dipole moment curves is evident and the agreement between ab initio data and NN model is quite good, which indicates the NN model can interpolate well in the quasi-degenerate region.

Along the loop with $\rho = 0.01$, the ab initio energy difference between the 1,2^{1}A states is about 250 cm^{-1}, which is very close to degeneracy. In the z-component dipole moment curves along this loop, noticeable differences between ab initio data and the NN model can be observed. The NH3ZY PEM predicts an energy difference of 48.3 cm^{-1} at the true degeneracy geometry in ab initio calculation. A small mismatch of the conical intersection location between the NH3ZY PEM and ab initio calculation may result in the difference in this figure. However, as for the loops with $\rho = 0.05$ and $\rho = 0.1$, as the energy differences become larger, which are about 1500 and 2500 cm^{-1} respectively, the effect of the mismatch fades away and the agreement between ab initio data and the NN model becomes better. The NH3ZY PEM provides a very accurate description of the conical intersection seam, and the mismatch only occurs in a small volume in the nuclear

DOI: 10.1021/acs.jctc.9b00898
J. Chem. Theory Comput. 2020, 16, 302−313

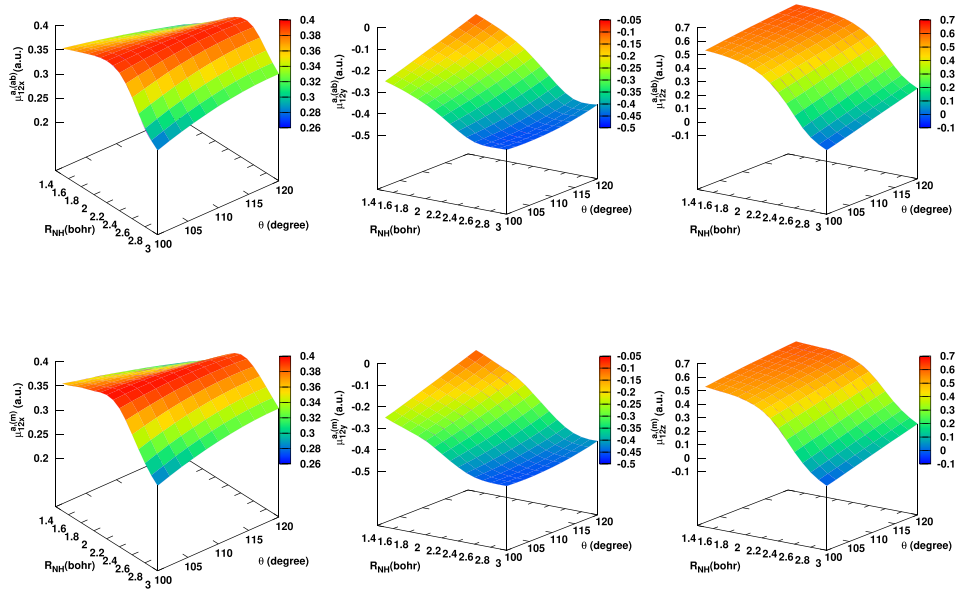

Figure 10. Comparison of ab initio (upper row) and NN model determined (lower row) adiabatic transition dipole moments near the energy minimum (C_{3v}) of 1^1A. The arbitrary signs of transition dipole moments have been manually adjusted to achieve smoothness. Each component is ploted as a function of R_{NH} and out-of-plane angle θ. θ is the angle between N−H bond and the C_3-axis.

coordinate space surrounding the seam, which will not affect the global quality of the NN DMSs.

In the framework of the Franck−Condon principle, the transition dipole moments are necessary to determine the probability amplitude between the ground vibronic state and the upper vibronic state. Therefore, the accurate reproduction of the transition dipole moments in the Franck−Condon region is of great importance for the simulations of absorption and emission spectroscopies.

The energy minimum of the 1^1A state is of C_{3v} symmetry, which is on the boundaries of the domain in which the DMSs are fit. The domain is defined by $R_{NH_1} \leq R_{NH_2} \leq R_{NH_3}$. On the boundaries, two or three NH bonds are equal. When evaluating the dipole and transition dipole on the boundaries, where the ordering of H atoms is not unique, the ordering used in the evaluation may not correspond to the ordering included in the fitting data, which leads to wrong predictions. In order to avoid such wrong predictions, when a geometry that has very similar NH bonds is encountered, the DMSs are not directly evaluated at this geometry. Instead, the relevant diabatized dipoles are obtained through Shepard interpolation[75,76] based on nearby geometries, and then the adiabatic dipole and transition dipole moments can be calculated. The details of Shepard interpolation can be found in Appendix B.

Figure 10 shows the transition dipole moments between the $1,2^1$A states near the energy minimum of 1^1A, in which the transition dipole moments are plotted on a 2D grid of an NH bond and the out-of-plane angle. The transition dipole moments are obtained through Shepard interpolation, since the 2D grid is on the boundaries of the domain. As can be seen in Figure 10 , the transition dipole moments have been well reproduced, and no wrong predictions can be seen, which also indicates the validity of the Shepard interpolation. Considering the high-level MRCISD calculations in use and that good reproduction of ab initio dipole moments has been achieved, the NN DMSs would be suitable for spectroscopy simulations, which will be completed in future work.

4. SUMMARY

In this work, we have constructed permanent dipole and transition dipole moment surfaces for the $1,2^1$A states of ammonia, which serve as an example of extending previous multistate coupled potential energy surface fitting to include auxiliary molecular properties. The DMSs are constructed by exploiting a previously reported accurate quasi-diabatic representation, NH3ZY PEM. The AtD transformation removes the discontinuities in electric dipole moments due to the conical intersections, which enables the fitting of diabatized dipole moments. Electric dipole moment is a vector property; the ideal functional form to rigorously account for molecular symmetry is difficult to design. However, by placing each geometry at a standard orientation, the functional form in use is greatly simplified. A cluster growing algorithm with Gaussian process regression is used to remove the arbitrariness in the signs of transition dipole moments. Finally, the diabatized dipole moments are represented with smooth NN functions. The NN DMSs can reproduce ab initio dipole moments very accurately; even the discontinuities at a conical intersection are well reproduced. The accurate NN DMSs are suitable for simulating IR and UV−Vis spectra of ammonia, which will be the subject of future work.

The results presented in this work also confirm the accuracy and validity of the NH3ZY PEM. It provides an accurate quasi-diabatic representation that could obtain smooth diabatized dipole moments, which makes the fitting possible. However, as mentioned previously, the NH3ZY PEM cannot reproduce the location of the conical intersection seam exactly, when diabatizing the dipole moments in quasi-degenerate regions; the small mismatch between the NH3ZY PEM and ab initio data leads to artificial discontinuities. To avoid these

DOI: 10.1021/acs.jctc.9b00898
J. Chem. Theory Comput. 2020, 16, 302−313

discontinuities, the quasi-degenerate points have to be excluded from the fitting. These artificial discontinuities are due to the fact that the construction of quasi-diabatic representation and the diabatization of dipole moments are done sequentially and separately. One possible solution for this mismatch is to diabatize the energies and dipole moments simultaneously, which could at least make the resulting quasi-diabatic representation and diabatized dipole moments consistent with each other. Another molecular interaction we are interested in is the spin−orbit coupling. Given the success of the diabatized dipole moments shown in this work, it is highly likely the spin−orbit couplings can also be diabatized and fitted. Through this work, we hope that, by including molecular properties/interactions in the construction of coupled potential energy surfaces, more chemical processes can be treated with accurate surface fitting methods.

APPENDIX A: CLUSTER GROWING ALGORITHM WITH GAUSSIAN PROCESS REGRESSION

The details of GPR are described in ref 58. In brief, GPR tries to model some latent function $y = f(\mathbf{x})$, where $\mathbf{x}$ is the N-dimensional input vector. At any input $\mathbf{x}$, there will be a conditional normal distribution $P(y)$ of function values y; given n known function values $\mathbf{y} = [y_1, ..., y_n]^T$ at n inputs $[\mathbf{x}_1, ..., \mathbf{x}_n]$. The mean of this conditional distribution at an arbitrary input $\mathbf{x}_*$ is given by

$$\mathbf{y}_* = \mathbf{k}_*^T \mathbf{K}^{-1} \mathbf{y} \tag{21}$$

where $\mathbf{k}_*$ is a vector with n components $k(\mathbf{x}_*, \mathbf{x}_i)$, and $\mathbf{K}$ is a square $n \times n$ matrix with elements $k(\mathbf{x}_i, \mathbf{x}_j)$. $k(\mathbf{x}_i, \mathbf{x}_j)$ is called the kernel function, which relates one data point $(y_i = f(\mathbf{x}_i))$ to another $(y_j = f(\mathbf{x}_j))$. Due to the explicit correlation between data points expressed by kernels, GPR has a certain limited capability to extrapolate beyond the known data set.[59] There are several kinds of kernel functions, and each kind has some free parameters. The optimal parameters can be estimated by maximizing the following log marginal likelihood:

$$\log \mathcal{L} = -\frac{1}{2}\mathbf{y}^T \mathbf{K}^{-1} \mathbf{y} - \frac{1}{2}\log |\mathbf{K}| - \frac{n}{2} \log 2\pi \tag{22}$$

In this work, each component of diabatized dipole moments is represented by a GPR model. Six coordinates including x_{H_1}, x_{H_2}, y_{H_2}, x_{H_3}, y_{H_3}, and z_{H_3} in the standard orientation are the input of GPR, since the other six Cartesian coordinates remain zero in the body-fixed Cartesian frame. Geometries are inverted in advance if necessary to have $z_{H_3} \geq 0$. By placing and inverting each geometry at its unique standard orientation, we could ignore the CNPI symmetry during cluster growing. At each iteration, the choice of nearby points is based on a distance criterion. The distances between points are computed as the Euclidean distance in the six-dimensional space of x_{H_1}, x_{H_2}, y_{H_2}, x_{H_3}, y_{H_3}, and z_{H_3}. The nearby points are found based on a cutoff threshold. The cutoff threshold is adjusted to a suitable value during each iteration. It should be neither too small nor too large. If it is too small, there will be very few points found nearby, and the cluster growing algorithm will need many iterations. If it is too large, the extrapolation of GPR may not be reliable at points far from the current cluster. The sign assignment of a new point is done through comparison between GPR predicted values and ab initio values with either positive or negative sign, and the sign that gives the smaller difference is chosen.

APPENDIX B: SHEPARD INTERPOLATION NEAR BOUNDARIES

When a geometry $\mathbf{x}_*$ near the boundaries is encountered, in order to perform Shepard interpolation, several nearby geometries are generated in the following way: first, this geometry is placed at standard orientation $\mathbf{x}'_*$; then, with all three H−N−H angles being fixed, three NH bonds are modified to have a small change (e.g., 0.02 or 0.05 bohr) to get away from the boundaries. The diabatized dipole moments at these nearby geometries are then evaluated in order to interpolate at $\mathbf{x}'_*$. Although these geometries do not necessarily satisfy the ascending bond lengths condition, their diabatized dipole moments can be obtained through permutation symmetry analyzed in section 2. For the geometries that do not satisfy the condition, H atoms are permuted to meet the requirement of ascending bond lengths. After permutation, the diabatized dipole moments can be readily evaluated from NN DMSs. According to the symmetry analysis of diabatized dipole moments in section 2, the diabatized dipole moments of unpermuted geometry can be easily obtained. In this work, a modified Shepard interpolation method[75,76] is used to obtain the diabatized dipole moments at $\mathbf{x}'_*$ with the three NH bond lengths being the independent variables.

AUTHOR INFORMATION

Corresponding Authors

*E-mail: yguan15@jhu.edu (Y.G.).
*E-mail: hguo@unm.edu (H.G.).
*E-mail: yarkony@jhu.edu (D.R.Y.).

ORCID

Hua Guo: 0000-0001-9901-053X
David R. Yarkony: 0000-0002-5446-1350

Funding

This work was supported by a National Science Foundation grant (CHE-1663692) to D.R.Y. H.G. acknowledges support from Department of Energy Grant No. DE-SC0015997.

Notes

The authors declare no competing financial interest.

ACKNOWLEDGMENTS

Computer resources for this work were provided by the Maryland Advanced Research Computing Center (MARCC).

REFERENCES

(1) Gatti, F. *Molecular Quantum Dynamics: from Theory to Applications*; Springer: Berlin, 2014.
(2) Guo, H.; Yarkony, D. R. Accurate nonadiabatic dynamics. *Phys. Chem. Chem. Phys.* **2016**, *18*, 26335−26352.
(3) Begušić, T.; Patoz, A.; Šulc, M.; Vaníček, J. On-the-fly ab initio three thawed Gaussians approximation: A semiclassical approach to Herzberg-Teller spectra. *Chem. Phys.* **2018**, *515*, 152−163.
(4) Zimmermann, T.; Vaníček, J. Evaluation of the importance of spin-orbit couplings in the nonadiabatic quantum dynamics with quantum fidelity and with its efficient "on-the-fly" ab initio semiclassical approximation. *J. Chem. Phys.* **2012**, *137*, 22A516.
(5) Mai, S.; Marquetand, P.; González, L. Nonadiabatic dynamics: The SHARC approach. *Wiley Interdiscip. Rev. Comput. Mol. Sci.* **2018**, *8*, No. e1370.
(6) Yurchenko, S. N.; Carvajal, M.; Lin, H.; Zheng, J.; Thiel, W.; Jensen, P. Dipole moment and rovibrational intensities in the

DOI: 10.1021/acs.jctc.9b00898
J. Chem. Theory Comput. 2020, 16, 302−313

electronic ground state of NH3: Bridging the gap between ab initio theory and spectroscopic experiment. *J. Chem. Phys.* **2005**, *122*, 104317.
(7) Yurchenko, S. N.; Yachmenev, A.; Thiel, W.; Baum, O.; Giesen, T. F.; Melnikov, V. V.; Jensen, P. An ab initio calculation of the vibrational energies and transition moments of HSOH. *J. Mol. Spectrosc.* **2009**, *257*, 57−65.
(8) Yurchenko, S. N. Electric dipole moments of small polyatomic molecules from first principles. *Chemical Modelling* **2013**, *10*, 183−228.
(9) Rheinecker, J. L.; Bowman, J. M. The calculated infrared spectrum of Cl-H_2O using a full dimensional ab initio potential surface and dipole moment surface. *J. Chem. Phys.* **2006**, *124*, 131102.
(10) Huang, X.; Fortenberry, R. C.; Wang, Y.; Francisco, J. S.; Crawford, T. D.; Bowman, J. M.; Lee, T. J. Dipole Surface and Infrared Intensities for the cis- and trans-HOCO and DOCO Radicals. *J. Phys. Chem. A* **2013**, *117*, 6932−6939.
(11) Wang, Y.; Carter, S.; Bowman, J. M. Variational Calculations of Vibrational Energies and IR Spectra of trans- and cis-HOCO Using New ab Initio Potential Energy and Dipole Moment Surfaces. *J. Phys. Chem. A* **2013**, *117*, 9343−9352.
(12) Wang, Y.; Bowman, J. M.; Kamarchik, E. Five ab initio potential energy and dipole moment surfaces for hydrated NaCl and NaF. I. Two-body interactions. *J. Chem. Phys.* **2016**, *144*, 114311.
(13) Chang, J.; Guo, L.; Wang, R.; Mou, J.; Ren, H.; Ma, J.; Guo, H. Absorption Spectra of Acetylene, Vinylidene, and Their Deuterated Isotopologues on Ab Initio Potential Energy and Dipole Moment Surfaces. *J. Phys. Chem. A* **2019**, *123*, 4232−4240.
(14) Yang, T.; Chen, J.; Huang, L.; Wang, T.; Xiao, C.; Sun, Z.; Dai, D.; Yang, X.; Zhang, D. H. Extremely short-lived reaction resonances in Cl + HD (v = 1) → DCl + H due to chemical bond softening. *Science* **2015**, *347*, 60−63.
(15) Kryachko, E. S.; Yarkony, D. R. Diabatic bases and molecular properties. *Int. J. Quantum Chem.* **2000**, *76*, 235−243.
(16) Baer, M. Adiabatic and diabatic representations for atom-diatom collisions: Treatment of the three-dimensional case. *Chem. Phys.* **1976**, *15*, 49−57.
(17) Mead, C. A.; Truhlar, D. G. Conditions for the definition of a strictly diabatic electronic basis for molecular systems. *J. Chem. Phys.* **1982**, *77*, 6090−6098.
(18) Baer, M. Introduction to the theory of electronic non-adiabatic coupling terms in molecular systems. *Phys. Rep.* **2002**, *358*, 75−142.
(19) Yarkony, D. R.; Xie, C.; Zhu, X.; Wang, Y.; Malbon, C. L.; Guo, H. Diabatic and adiabatic representations: Electronic structure caveats. *Comput. Theor. Chem.* **2019**, *1152*, 41−52.
(20) Subotnik, J. E.; Yeganeh, S.; Cave, R. J.; Ratner, M. A. Constructing diabatic states from adiabatic states: Extending generalized Mulliken−Hush to multiple charge centers with Boys localization. *J. Chem. Phys.* **2008**, *129*, 244101.
(21) Hoyer, C. E.; Parker, K.; Gagliardi, L.; Truhlar, D. G. *J. Chem. Phys.* **2016**, *144*, 194101.
(22) Nakamura, H.; Truhlar, D. G. Direct diabatization of electronic states by the fourfold way. II. Dynamical correlation and rearrangement processes. *J. Chem. Phys.* **2002**, *117*, 5576−5593.
(23) Nakamura, H.; Truhlar, D. G. Extension of the fourfold way for calculation of global diabatic potential energy surfaces of complex, multiarrangement, non-Born-Oppenheimer systems: Application to HNCO(S_0,S_1). *J. Chem. Phys.* **2003**, *118*, 6816−6829.
(24) Lenzen, T.; Manthe, U. Neural network based coupled diabatic potential energy surfaces for reactive scattering. *J. Chem. Phys.* **2017**, *147*, No. 084105.
(25) Williams, D. M. G.; Eisfeld, W. Neural network diabatization: A new ansatz for accurate high-dimensional coupled potential energy surfaces. *J. Chem. Phys.* **2018**, *149*, 204106.
(26) Berry, M. V. Quantal phase factors accompanying adiabatic changes. *Proc. R. Soc. London, Ser. A* **1984**, *392*, 45−57.
(27) Yarkony, D. R. On the consequences of nonremovable derivative couplings. I. The geometric phase and quasidiabatic states: A numerical study. *J. Chem. Phys.* **1996**, *105*, 10456−10461.
(28) Malbon, C. L.; Zhu, X.; Guo, H.; Yarkony, D. R. On the incorporation of the geometric phase in general single potential energy surface dynamics: A removable approximation to ab initio data. *J. Chem. Phys.* **2016**, *145*, 234111.
(29) Ryabinkin, I. G.; Izmaylov, A. F. Geometric Phase Effects in Dynamics Near Conical Intersections: Symmetry Breaking and Spatial Localization. *Phys. Rev. Lett.* **2013**, *111*, 220406.
(30) Izmaylov, A. F. Perturbative wave-packet spawning procedure for non-adiabatic dynamics in diabatic representation. *J. Chem. Phys.* **2013**, *138*, 104115.
(31) Ryabinkin, I. G.; Joubert-Doriol, L.; Izmaylov, A. F. When do we need to account for the geometric phase in excited state dynamics? *J. Chem. Phys.* **2014**, *140*, 214116.
(32) Gherib, R.; Ryabinkin, I. G.; Izmaylov, A. F. Why Do Mixed Quantum-Classical Methods Describe Short-Time Dynamics through Conical Intersections So Well? Analysis of Geometric Phase Effects. *J. Chem. Theory Comput.* **2015**, *11*, 1375−1382.
(33) Gherib, R.; Ye, L.; Ryabinkin, I. G.; Izmaylov, A. F. On the inclusion of the diagonal Born-Oppenheimer correction in surface hopping methods. *J. Chem. Phys.* **2016**, *144*, 154103.
(34) Yarkony, D. R. Conical Intersections: Diabolical and Often Misunderstood. *Acc. Chem. Res.* **1998**, *31*, 511−518.
(35) Yarkony, D. R. On the adiabatic to diabatic states transformation near intersections of conical intersections. *J. Chem. Phys.* **2000**, *112*, 2111−2120.
(36) Yarkony, D. R. On the characterization of regions of avoided surface crossings using an analytic gradient based method. *J. Chem. Phys.* **1990**, *92*, 2457−2463.
(37) Köppel, H. *Conical Intersections*; World Scientific: Singapore, 2011; pp 175−204.
(38) Sadygov, R. G.; Yarkony, D. R. On the adiabatic to diabatic states transformation in the presence of a conical intersection: A most diabatic basis from the solution to a Poisson's equation. I. *J. Chem. Phys.* **1998**, *109*, 20−25.
(39) Abrol, R.; Kuppermann, A. An optimal adiabatic-to-diabatic transformation of the $1_2A'$ and $2_2A'$ states of H_3. *J. Chem. Phys.* **2002**, *116*, 1035−1062.
(40) Yuan, D.; Guan, Y.; Chen, W.; Zhao, H.; Yu, S.; Luo, C.; Tan, Y.; Xie, T.; Wang, X.; Sun, Z.; Zhang, D. H.; Yang, X. Observation of the geometric phase effect in the H + HD → H_2 + D reaction. *Science* **2018**, *362*, 1289−1293.
(41) Evenhuis, C. R.; Collins, M. A. Interpolation of diabatic potential energy surfaces. *J. Chem. Phys.* **2004**, *121*, 2515−2527.
(42) Godsi, O.; Evenhuis, C. R.; Collins, M. A. Interpolation of multidimensional diabatic potential energy matrices. *J. Chem. Phys.* **2006**, *125*, 104105.
(43) Evenhuis, C.; Martínez, T. J. A scheme to interpolate potential energy surfaces and derivative coupling vectors without performing a global diabatization. *J. Chem. Phys.* **2011**, *135*, 224110.
(44) Mukherjee, S.; Bandyopadhyay, S.; Paul, A. K.; Adhikari, S. Construction of Diabatic Hamiltonian Matrix from ab Initio Calculated Molecular Symmetry Adapted Nonadiabatic Coupling Terms and Nuclear Dynamics for the Excited States of Na3 Cluster. *J. Phys. Chem. A* **2013**, *117*, 3475−3495.
(45) Baer, M. *Beyond Born-Oppenheimer*; John Wiley & Sons: Hoboken, NJ; 2006.
(46) Zhu, X.; Yarkony, D. R. Toward eliminating the electronic structure bottleneck in nonadiabatic dynamics on the fly: An algorithm to fit nonlocal, quasidiabatic, coupled electronic state Hamiltonians based on ab initio electronic structure data. *J. Chem. Phys.* **2010**, *132*, 104101.
(47) Zhu, X.; Yarkony, D. R. On the representation of coupled adiabatic potential energy surfaces using quasi-diabatic Hamiltonians: A distributed origins expansion approach. *J. Chem. Phys.* **2012**, *136*, 174110.
(48) Zhu, X.; Yarkony, D. R. Quasi-diabatic representations of adiabatic potential energy surfaces coupled by conical intersections including bond breaking: A more general construction procedure and

DOI: 10.1021/acs.jctc.9b00898
J. Chem. Theory Comput. 2020, 16, 302−313

an analysis of the diabatic representation. *J. Chem. Phys.* **2012**, *137*, 22A511.
(49) Zhu, X.; Yarkony, D. R. Fitting coupled potential energy surfaces for large systems: Method and construction of a 3-state representation for phenol photodissociation in the full 33 internal degrees of freedom using multireference configuration interaction determined data. *J. Chem. Phys.* **2014**, *140*, No. 024112.
(50) Ma, J.; Zhu, X.; Guo, H.; Yarkony, D. R. First principles determination of the $NH_2/ND_2(\tilde{A}/\tilde{X})$ branching ratios for photodissociation of NH3/ND3 via full-dimensional quantum dynamics based on a new quasi-diabatic representation of coupled ab initio potential energy surfaces. *J. Chem. Phys.* **2012**, *137*, 22A541.
(51) Ma, J.; Xie, C.; Zhu, X.; Yarkony, D. R.; Xie, D.; Guo, H. Full-Dimensional Quantum Dynamics of Vibrationally Mediated Photodissociation of NH_3 and ND_3 on Coupled Ab Initio Potential Energy Surfaces: Absorption Spectra and $NH2(\tilde{A}^2A_1/NH_2(\tilde{X}^2B_1)$ Branching Ratios. *J. Phys. Chem. A* **2014**, *118*, 11926−11934.
(52) Xie, C.; Ma, J.; Zhu, X.; Zhang, D. H.; Yarkony, D. R.; Xie, D.; Guo, H. Full-Dimensional Quantum State-to-State Nonadiabatic Dynamics for Photodissociation of Ammonia in its ABand. *J. Phys. Chem. Lett.* **2014**, *5*, 1055−1060.
(53) Xie, C.; Zhu, X.; Ma, J.; Yarkony, D. R.; Xie, D.; Guo, H. Communication: On the competition between adiabatic and nonadiabatic dynamics in vibrationally mediated ammonia photodissociation in its A band. *J. Chem. Phys.* **2015**, *142*, No. 091101.
(54) Guan, Y.; Zhang, D. H.; Guo, H.; Yarkony, D. R. Representation of coupled adiabatic potential energy surfaces using neural network based quasi-diabatic Hamiltonians: 1,2 ^{2}A' states of LiFH. *Phys. Chem. Chem. Phys.* **2019**, *21*, 14205−14213.
(55) Guan, Y.; Guo, H.; Yarkony, D. R. Neural network based quasi-diabatic Hamiltonians with symmetry adaptation and a correct description of conical intersections. *J. Chem. Phys.* **2019**, *150*, 214101.
(56) Bunker, P. R.; Jensen, P. *Molecular Symmetry and Spectroscopy*; NRC Research Press: 2006.
(57) Shu, Y.; Kryven, J.; Sampaio de Oliveira-Filho, A. G.; Zhang, L.; Song, G.-L.; Li, S. L.; Meana-Pañeda, R.; Fu, B.; Bowman, J. M.; Truhlar, D. G. Direct Diabatization and Analytic Representation of Coupled Potential Energy Surfaces and Couplings for the Reactive Quenching of the Excited $^2\Sigma^+$ State of OH by Molecular Hydrogen. *J. Chem. Phys.* **2019**, *151*, 104311.
(58) Williams, C. K.; Rasmussen, C. E. *Gaussian Processes for Machine Learning*; MIT Press: Cambridge, MA, 2006; Vol. *2*.
(59) Vargas-Hernández, R. A.; Sous, J.; Berciu, M.; Krems, R. V. Extrapolating Quantum Observables with Machine Learning: Inferring Multiple Phase Transitions from Properties of a Single Phase. *Phys. Rev. Lett.* **2018**, *121*, 255702.
(60) Raff, L.; Komanduri, R.; Hagan, M.; Bukkapatnam, S. *Neural Networks in Chemical Reaction Dynamics*; Oxford University Press: 2012.
(61) Kondati Natarajan, S.; Morawietz, T.; Behler, J. Representing the potential-energy surface of protonated water clusters by high-dimensional neural network potentials. *Phys. Chem. Chem. Phys.* **2015**, *17*, 8356−8371.
(62) Xie, C.; Zhu, X.; Yarkony, D. R.; Guo, H. Permutation invariant polynomial neural network approach to fitting potential energy surfaces. IV. Coupled diabatic potential energy matrices. *J. Chem. Phys.* **2018**, *149*, 144107.
(63) Braams, B. J.; Bowman, J. M. Permutationally invariant potential energy surfaces in high dimensionality. *Int. Rev. Phys. Chem.* **2009**, *28*, 577−606.
(64) Bowman, J. M.; Czakó, G.; Fu, B. High-dimensional ab initio potential energy surfaces for reaction dynamics calculations. *Phys. Chem. Chem. Phys.* **2011**, *13*, 8094−8111.
(65) Hagan, M. T.; Menhaj, M. B. Training feedforward networks with the Marquardt algorithm. *IEEE Transactions on Neural Networks* **1994**, *5*, 989−993.
(66) https://github.com/virtualzx-nad/NH3-X-A-Coupled-PES.
(67) Lischka, H.; Shepard, R.; Pitzer, R. M.; Shavitt, I.; Dallos, M.; Müller, T.; Szalay, P. G.; Seth, M.; Kedziora, G. S.; Yabushita, S.; Zhang, Z. High-level multireference methods in the quantum-chemistry program system COLUMBUS: Analytic MR-CISD and MR-AQCC gradients and MR-AQCC-LRT for excited states, GUGA spin−orbit CI and parallel CI density. *Phys. Chem. Chem. Phys.* **2001**, *3*, 664−673.
(68) Lischka, H.; Dallos, M.; Szalay, P. G.; Yarkony, D. R.; Shepard, R. Analytic evaluation of nonadiabatic coupling terms at the MR-CI level. I. Formalism. *J. Chem. Phys.* **2004**, *120*, 7322−7329.
(69) Byrd, R.; Lu, P.; Nocedal, J.; Zhu, C. A Limited Memory Algorithm for Bound Constrained Optimization. *SIAM Journal on Scientific Computing* **1995**, *16*, 1190−1208.
(70) Agrafiotis, D. K.; Cedeño, W.; Lobanov, V. S. On the Use of Neural Network Ensembles in QSAR and QSPR. *J. Chem. Inf. Comput. Sci.* **2002**, *42*, 903−911.
(71) Zhou, Z.; Wu, J.; Tang, W. Ensembling neural networks: Many could be better than all. *Artif. Intell.* **2002**, *137*, 239−263.
(72) Li, J.; Jiang, B.; Guo, H. Permutation invariant polynomial neural network approach to fitting potential energy surfaces. II. Four-atom systems. *J. Chem. Phys.* **2013**, *139*, 204103.
(73) Xu, X.; Chen, J.; Zhang, D. H. Global Potential Energy Surface for the $H+CH_4 \leftrightarrow H_2+CH_3$ Reaction using Neural Networks. *Chin. J. Chem. Phys.* **2014**, *27*, 373−379.
(74) Atchity, G. J.; Xantheas, S. S.; Ruedenberg, K. Potential energy surfaces near intersections. *J. Chem. Phys.* **1991**, *95*, 1862−1876.
(75) Renka, R. J. Multivariate Interpolation of Large Sets of Scattered Data. *ACM Trans. Math. Softw.* **1988**, *14*, 139−148.
(76) Renka, R. J. Algorithm 661: QSHEP3D: Quadratic Shepard method for trivariate interpolation of scattered data. *ACM Trans. Math. Softw.* **1988**, *14*, 151−152.
(77) Grisafi, A.; Wilkins, D. M.; Csányi, G.; Ceriotti, M. Symmetry-adapted machine learning for tensorial properties of atomistic systems. *Phys. Rev. Lett.* **2018**, *120*, 036002.
(78) Wilkins, D. M.; Grisafi, A.; Yang, Y.; Lao, K. U.; DiStasio, R. A.; Ceriotti, M. Accurate molecular polarizabilities with coupled cluster theory and machine learning. *Proc. Natl. Acad. Sci. U. S. A.* **2019**, *116*, 3401−3406.

DOI: 10.1021/acs.jctc.9b00898
J. Chem. Theory Comput. 2020, 16, 302−313